International Journal of Solids and Structures 46 (2009) 2724–2738

Contents lists available at ScienceDirect

International Journal of Solids and Structures

journal homepage: www.elsevier.com/locate/ijsolstr

Superelasticity and stability of a shape memory alloy hexagonal honeycomb under in-plane compression

P.A. Michailidis [a], N. Triantafyllidis [a,*], J.A. Shaw [a], D.S. Grummon [b]

[a] The University of Michigan, Aerospace Engineering Department, Ann Arbor, MI 48109-2140, USA
[b] Michigan State University, Department of Chemical Engineering & Materials Science, East Lansing, MI 48824, USA

ARTICLE INFO

Article history:
Received 10 September 2008
Received in revised form 4 March 2009
Available online 25 March 2009

Keywords:
Shape memory alloy
Finite element analysis
Honeycomb
Instability
Bloch wave

ABSTRACT

Nitinol (NiTi) shape memory alloy honeycombs, fabricated in low densities using a new brazing method [Grummon, D., Shaw, J., Foltz, J., 2006. Fabrication of cellular shape memory alloy materials by reactive eutectic brazing using niobium. Materials Science and Engineering A 438–440, 1113–1118], recently demonstrated enhanced shape memory and superelastic properties [Shaw, J. A., Grummon, D. S., Foltz, J., 2007b. Superelastic NiTi honeycombs: Fabrication and experiments. Smart Materials and Structures 16, S170–S178] by exploiting kinematic amplification of thin-walled deformations. The realization of such adaptive, light-weight cellular structures opens interesting possibilities for design and novel applications. This paper addresses the consequent need for design and simulation tools for engineers to make effective use of such structures by, as a first step, analyzing the multi-scale stability aspects of the superelastic behavior of a particular hexagonal, thin-walled, SMA honeycomb under in-plane compression. An in-depth parameter study is performed of the influence of different material laws on the behavior of honeycombs of finite and infinite extent with perfect and imperfect initial geometries. A finite element-based simulation is presented that credibly captures the behavior seen in experiments.

© 2009 Elsevier Ltd. All rights reserved.

1. Introduction

Low density cellular solids, particularly metallic ones, are widely used in engineering applications (Gibson and Ashby, 1997; Ashby et al., 2000), since they can be designed to have high stiffness-to-mass ratios and desirable energy absorption characteristics. Cellular structures made from shape memory alloys (SMA's) are especially interesting for their potential to deliver superelasticity and shape memory in a light-weight material. While porous forms of NiTi (Nitinol) have been produced (Li et al., 1999; Lagoudas and Vandygriff, 2002; Grummon et al., 2002), the difficulty of joining Nitinol to itself has historically prevented the fabrication of NiTi-based cellular honeycombs with useful adaptive properties. Other attempts to fabricate SMA honeycombs have been done by mechanical fasteners or gluing (Hassan et al., 2004; Okabe et al., 2008), and a few modeling and design studies, focusing mostly on stiffness and Poisson ratio, have been performed (Freed et al., 2008).

An enabling metallurgical bonding method was discovered recently, however, by Grummon et al. (2006), which led to the construction and testing of the first NiTi honeycomb specimens showing robust properties. Two different cell geometries, hexagonal and wavy-corrugated, were produced by shape setting NiTi strips into corrugated forms, bonding them together at high temperature using a Niobium-based braze, and then heat-treating the resulting structures at moderate temperature. Compressive isothermal experiments on the specimens exhibited superelasticity with over macroscopic 50% strain recovery (Shaw et al., 2007b), and non-isothermal shape memory experiments demonstrated stress-free recovery of similar macroscopic strains (Shaw et al., 2007a).

A low-density cellular architecture made of an SMA has several advantages. The maximum tensile strain recovery of a monolithic Nitinol polycrystal is in the range of 5–8% in the low-cycle limit and less than 2.5% for high cycle loading. These limits can be substantially amplified structurally by exploiting bending of the thin walls in an open cell topology. Moreover, thermal inertia, which tends to dominate the response time of SMA actuators and cause hypersensitive superelastic rate-dependencies (see, for example, Shaw and Kyriakides, 1995; Shaw and Kyriakides, 1997; Iadicola and Shaw, 2004), scales with the material's volume-to-surface ratio and can thus be potentially reduced by adopting a low-density architecture. Considering these advantages, the goal of the present work is to explore in detail the isothermal, superelastic response of a hexagonal unit cell, to investigate the instabilities of the overall honeycomb structure under compressive loading–unloading, and to study the influence of different material properties and imperfections at various scales.

* Corresponding author. Tel.: +1 734 763 2356; fax: +1 734 763 0578.
E-mail address: nick@umich.edu (N. Triantafyllidis).

0020-7683/$ - see front matter © 2009 Elsevier Ltd. All rights reserved.
doi:10.1016/j.ijsolstr.2009.03.013

The presentation of the work is outlined as follows. Section 2 presents the kinematic structural model, the material model, and the methods used to establish the stability of the infinite (using Bloch waves) and finite (perfect and imperfect) honeycombs. Section 3 describes the numerical approach and material parameters used. Simulation results are presented in Section 4, which investigates the choice of constitutive model parameters and then demonstrates the responses of infinite-perfect, finite-perfect and finite geometrically imperfect honeycomb structures. The section ends with the selection of material parameters for a finite element simulation of an experiment on a fabricated SMA honeycomb. Lastly, summary and conclusions are provided in Section 5.

2. Modeling

The structural and material models employed in numerical simulations of in-plane compression are presented in this section. The first part presents the geometry of the honeycomb structure and the kinematics of cell wall deformation. The second part describes the constitutive model for isothermal, superelastic deformations. The last part describes the methods and criteria to determine stability of infinite-perfect, finite-perfect and finite-imperfect honeycomb structures.

2.1. Kinematics

A typical planar section of a perfectly periodic honeycomb, consisting of a regular hexagonal lattice, is shown in the undeformed (reference) configuration in Fig. 1(a). The cell walls have thickness t (except for $2t$ along the X_1 direction) and length L. A cutout of a periodic unit cell is also shown in the figure, which is used for stability calculations discussed later in Section 2.3. In all simulations of this paper the aspect ratio of cell wall thickness to length was fixed at $t/L = 1/30$, corresponding to one of the hexagonal honeycombs presented in Shaw et al. (2007b). Upon in-plane mechanical compression (for now, we consider loading along the X_2-axis), the cell walls deform primarily through bending with some axial loading, so each ligament is idealized as a small strain, nonlinear beam capable of sustaining arbitrarily large displacements and rotations. The structural model has already been presented elsewhere (see Triantafyllidis and Schraad, 1998), but for completeness, a brief description is included below.

Consider an initially straight beam of length l and thickness t as shown in Fig. 1(b) (with unit out-of-plane width). During loading, a material point initially at local axial coordinate x on the beam's undeformed mid-line (dotted line) moves to a new position on the deformed mid-line by displacements $v(x)$ and $w(x)$ along the local tangential (x) and normal (y) directions of the initial configuration, respectively. By adopting the classic Bernoulli–Euler assumption where cross-sections normal to the undeformed mid-line remain normal in its deformed counterpart and undergo small strain extension, the axial strain of a material point with initial local coordinates (x,y) is given by

$$\varepsilon(x,y) = e(x) + y\kappa(x), \tag{2.1}$$

where the mid-line axial strain $e(x)$ and the bending curvature $\kappa(x)$ are expressed in terms of the displacements $v(x)$ and $w(x)$ by

$$e = \left[\left(1+\frac{dv}{dx}\right)^2 + \left(\frac{dw}{dx}\right)^2\right]^{1/2} - 1,$$
$$\kappa = \left[\frac{dw}{dx}\frac{d^2v}{dx^2} - \left(1+\frac{dv}{dx}\right)\frac{d^2w}{dx^2}\right] \Big/ \left[\left(1+\frac{dv}{dx}\right)^2 + \left(\frac{dw}{dx}\right)^2\right]. \tag{2.2}$$

The contribution of internal virtual work from each ligament in the weak form of the equilibrium equations is given by

$$\delta W_l^l = \int_0^l (N\delta e + M\delta\kappa)dx; \quad \text{with } N \equiv \int_{-t/2}^{t/2}\sigma\, dy, \quad \text{and } M \equiv \int_{-t/2}^{t/2}\sigma y\, dy, \tag{2.3}$$

where $N(x)$ and $M(x)$ are the axial force and bending moment resultants, respectively, and $\sigma(x,y)$ is the local axial stress in the cell wall. The Euler–Lagrange equations corresponding to 2.1, 2.2 and 2.3 have been shown to coincide with the exact equilibrium equations of the beam in the current configuration, thus making this structural theory a consistent one (the interested reader is referred to Triantafyllidis and Samanta (1986), for a detailed discussion).

2.2. Constitutive model

Since only isothermal deformations of the SMA honeycomb are presently considered (consistent with slow superelastic loading–

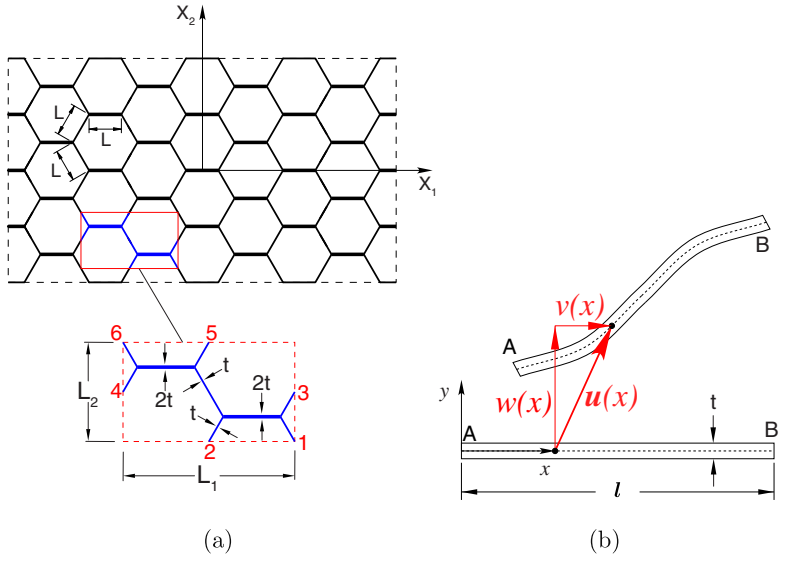

Fig. 1. (a) Reference configuration geometry and global coordinates (X_1,X_2) of the perfect SMA honeycomb. The honeycomb is compressed along the X_2 direction. The magnified view is the periodic unit cell used in stability calculations for the infinite-perfect honeycomb. (b) Kinematics of cell-wall deformations with respect to local coordinates (x,y), showing displacements (v,w) between reference configuration (AB) and current configuration ($A'B'$).

unloading), a small strain, one-dimensional, rate-independent, isothermal, hysteretic, constitutive model is described below. As is common in SMA modeling, an internal variable formulation is used to describe the extent of stress-induced phase transformation. The uniaxial constitutive model employed here has only one internal variable $\xi \in [0,1]$, which represents the martensite phase fraction at a material point (x,y). Pure austenite (A) and pure martensite, either tensile M^+ or compressive M^-, are represented by $\xi = 0$ and $\xi = 1$, respectively.[1] We note that the constitutive model has similarities to a conventional elasto-plastic constitutive law, but it has important differences in that the internal field variable is bounded in our case, unlike plasticity, and the unloading behavior is quite different, leading to superelasticity in our case. Both differences lead to interesting stability changes in the honeycomb structure, as will be shown in Section 4, where stability can be lost but then regained as phase transformation saturates in either direction. Furthermore, this model can be readily generalized to include temperature-induced transformations and consequent shape memory behavior, although this is left for future work.

In its simplest form the constitutive law for the local stress, $\sigma(x,y)$, is

$$\sigma = \begin{cases} E(\varepsilon - \beta^+\xi), & \text{for } \varepsilon \geqslant 0 \\ E(\varepsilon - \beta^-\xi), & \text{for } \varepsilon < 0 \end{cases} \tag{2.4}$$

where $\varepsilon(x,y)$ is the local fiber strain corresponding to Eq. (2.1) and $\xi(x,y)$ is the local fiber martensite phase fraction. The remaining parameters are material constants, in which, E is the effective uniaxial elastic modulus[2] (phase independent, here) and β^+ and β^- are the respective transformation strains (material constants) in tension and compression[3]. Allowing different transformation behavior in compression vs. tension provides the flexibility to capture tension–compression asymmetry, which is a known phenomenon in textured SMA polycrystals (Gall et al., 1999). For elastic loading–unloading the internal variable ξ remains constant, i.e., $\dot{\xi} = 0$ (where $(\dot{\cdot})$ denotes the time derivative $d(\,)/dt$). The onset of phase transformation during mechanical loading from $A \to M$ occurs at a nucleation strain of ε_n^+ in tension ($\varepsilon > 0$ and $\dot{\varepsilon} > 0$) or ε_n^- in compression ($\varepsilon < 0$ and $\dot{\varepsilon} < 0$). Phase transformation evolves along two-phase stress paths (see Fig. 2) according to

$$\sigma = \begin{cases} \hat{\sigma}_l^+(\xi), & \text{for } A \to M^+ \\ \hat{\sigma}_u^+(\xi), & \text{for } A \leftarrow M^+ \\ \hat{\sigma}_u^-(\xi), & \text{for } A \leftarrow M^- \\ \hat{\sigma}_l^-(\xi), & \text{for } A \to M^-, \end{cases} \tag{2.5}$$

where subscripts l and u refer to "loading" and "unloading", respectively, in the sense that "loading" is associated with the direction $A \to M$ (either M^+ or M^-). Phase transformation hysteresis is parameterized with material constants $\Delta\sigma_A^+, \Delta\sigma_M^+, \Delta\sigma_A^-, \Delta\sigma_M^-$. Loading and unloading paths are related by

$$\begin{aligned} \hat{\sigma}_l^+(\xi) &= \hat{\sigma}_u^+(\xi) + (1-\xi)\Delta\sigma_A^+ + \xi\Delta\sigma_M^+ \\ \hat{\sigma}_u^-(\xi) &= \hat{\sigma}_l^-(\xi) + (1-\xi)\Delta\sigma_A^- + \xi\Delta\sigma_M^- \end{aligned} \tag{2.6}$$

[1] We assume that the temperature is sufficiently high such that M^- and M^+ never exist simultaneously at any material point.

[2] We have assumed the local stress to be purely uniaxial, so E is to be interpreted as the Young's modulus if the ligament out-of-plane depth is small. If the ligament depth cannot be neglected, as is the case for the actual honeycomb specimen considered later, it can alternatively be interpreted approximately as the modulus for cylindrical plate bending, $E/(1-\nu^2)$, consistent with our 2-D context. In any case, the results in this work are presented in dimensionless form where stresses have been normalized by E.

[3] From here on, quantities associated with the tensile or compressive behavior are denoted by a + or − superscript, respectively. Absence of the + or − superscript means that the parameter applies to both tensile and compressive parts of the constitutive behavior.

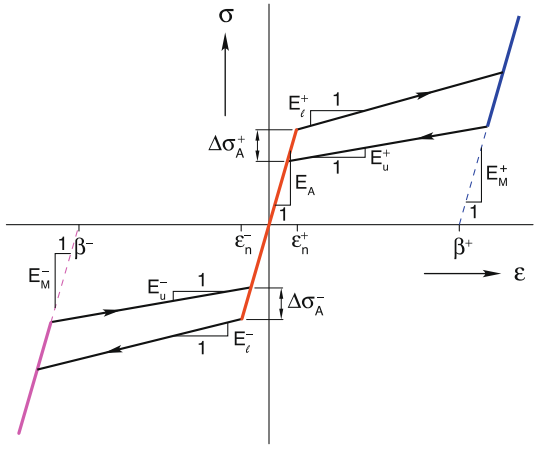

Fig. 2. Uniaxial superelastic response of SMA material and associated constitutive parameters. Subscripts A or M refer to Austenite or Martensite while superscripts $(\cdot)^+$ or $(\cdot)^-$ indicate association with tensile or compressive response, respectively.

where $\Delta\sigma_M^+(\Delta\sigma_M^-)$ is related to $\Delta\sigma_A^+(\Delta\sigma_A^-)$ and the loading, unloading tangent moduli in tension (compression) E_l^+, E_u^+ (E_l^-, E_u^-) by

$$\begin{aligned} \Delta\sigma_M^+ &= \Delta\sigma_A^+ + \beta^+\left[1/(1/E_l^+ - 1/E) - 1/(1/E_u^+ - 1/E)\right] \\ \Delta\sigma_M^- &= \Delta\sigma_A^- + \beta^-\left[1/(1/E_l^- - 1/E) - 1/(1/E_u^- - 1/E)\right] \end{aligned} \tag{2.7}$$

For simplicity the functions $\hat{\sigma}(\xi)$, are chosen such that the tangent moduli during the loading (E_l) or unloading (E_u) phase transformation are material constants.[4] Consequently

$$\dot{\xi} = \begin{cases} \frac{E-E_l^+}{E}\frac{\dot{\varepsilon}}{\beta^+}: & \text{if } \dot{\varepsilon} > 0,\ \sigma = \hat{\sigma}_l^+(\xi), \quad \text{and } \xi < 1 \\ \frac{E-E_u^+}{E}\frac{\dot{\varepsilon}}{\beta^+}: & \text{if } \dot{\varepsilon} < 0,\ \sigma = \hat{\sigma}_u^+(\xi), \quad \text{and } \xi > 0 \\ \frac{E-E_l^-}{E}\frac{\dot{\varepsilon}}{\beta^-}: & \text{if } \dot{\varepsilon} < 0,\ \sigma = \hat{\sigma}_l^-(\xi), \quad \text{and } \xi < 1 \\ \frac{E-E_u^-}{E}\frac{\dot{\varepsilon}}{\beta^-}: & \text{if } \dot{\varepsilon} > 0,\ \sigma = \hat{\sigma}_u^-(\xi), \quad \text{and } \xi > 0 \end{cases} \tag{2.8}$$

All the constants involved in the definition of the constitutive law are shown in Fig. 2. Specific values of the material constants will be chosen in Section 4.

2.3. Stability of the SMA honeycomb structure

A deep understanding of the behavior of the SMA honeycomb structure requires the investigation of its stability. Specifically, we seek the stability of the principal solutions of the infinite and finite perfect structures, both having equilibrium solutions where all unit cells undergo identical (periodic) deformations. The stability of the former is studied with the help of Bloch wave representation theory while the stability of the latter includes the effects of boundary conditions on the finite structure. Both are key ingredients to help explain the behavior of the actual finite, imperfect SMA structure.

Based on the constitutive model formulated, we are interested in the stability of the principal equilibrium path of a rate-independent, yet path-dependent, "elastoplastic" solid. Following Hill, 1958, the stability of the rate-independent solid considered here is governed by the criterion of positive definiteness of the quadratic functional[5,6]

[4] When $E_u^+ = E_l^+ (E_u^- = E_l^-)$ the corresponding tangent modulus during phase transformation is denoted by E_t^+ (E_t^-).

[5] From here on bold-face symbols denote vectors and matrices while a $(\bullet)$ denotes a simple contraction (inner product).

[6] The superscript $(*)$ denotes complex conjugation of the transpose quantity. The extension to the complex domain of the quadratic form associated with the stability of the structure enables the efficient use of the Bloch wave representation theorem.

$$\varphi(\lambda, \Delta\mathbf{u}) = \Delta\mathbf{u}^* \bullet \mathbf{K}(\lambda) \bullet \Delta\mathbf{u}, \tag{2.9}$$

where $\mathbf{K}$ is the incremental stiffness matrix of the structure evaluated at an equilibrium solution along the principal path, which is a function of the scalar parameter λ, and $\Delta\mathbf{u}$ is any kinematically admissible generalized displacement perturbation (i.e. contains displacement as well as rotation degrees of freedom).

2.3.1. Stability of the infinite, perfect honeycomb

Making use of the periodicity of the principal solution and using static condensation to eliminate internal degrees of freedom (DOFs) of the unit cell, the stability of the infinite structure requires the positive definiteness of the quadratic form defined on the unit cell

$$\hat{\varphi}(\lambda, \Delta\mathbf{u}) = \sum_{i,j=1}^{6} \Delta\mathbf{u}_i^* \bullet \mathbf{K}_{ij}(\lambda) \bullet \Delta\mathbf{u}_j, \tag{2.10}$$

where the 4×4 stiffness matrix $\mathbf{K}_{ij}$ is associated with the generalized force perturbation at boundary node i of the unit cell due to generalized displacement perturbation $\Delta\mathbf{u}_j$ at boundary node j (see again Fig. 1(a) for the numbering of the six exterior unit cell nodes). The stability investigation further requires the Bloch wave representation theory for the displacement perturbations, since it probes all wavelengths and directions. This approach simplifies the problem considerably, since it requires only the incremental response of the unit cell. Although the corresponding methodology is explained in detail in Triantafyllidis and Schnaidt (1993) for rectangular grillages, Triantafyllidis and Schraad (1998) for hexagonal honeycomb structures and Triantafyllidis et al. (2006) for the continuum case, a brief description is included here for completeness.

From Bloch wave representation theory the generalized displacement perturbation $\Delta\mathbf{u}$ takes the form

$$\Delta\mathbf{u}(X_1, X_2) = \exp[i(\omega_1 X_1 + \omega_2 X_2)]\mathbf{p}(X_1, X_2), \tag{2.11}$$

where $i = \sqrt{-1}$, ω_I is the wavenumber of the perturbation along the direction X_I, and $\mathbf{p}(\mathbf{X})$ is a doubly periodic complex-valued vector function of the spatial coordinates X_1 and X_2 with periods equal to the unit cell dimensions, i.e. $\mathbf{p}(X_1,X_2) = \mathbf{p}(X_1 + m_1L_1, X_2 + m_2L_2)$ for any pair of integers (m_1,m_2).

From (2.11) one deduces the following relation between the displacement perturbations at the boundary nodes

$$\begin{bmatrix} \Delta\mathbf{u}_4 \\ \Delta\mathbf{u}_5 \\ \Delta\mathbf{u}_6 \end{bmatrix} = \begin{bmatrix} \mathbf{0} & \mathbf{0} & \exp(-i\omega_1 L_1)\mathbf{I} \\ \mathbf{0} & \exp(i\omega_2 L_2)\mathbf{I} & \mathbf{0} \\ \exp(-i\omega_1 L_1 + i\omega_2 L_2)\mathbf{I} & \mathbf{0} & \mathbf{0} \end{bmatrix} \begin{bmatrix} \Delta\mathbf{u}_1 \\ \Delta\mathbf{u}_2 \\ \Delta\mathbf{u}_3 \end{bmatrix} \tag{2.12}$$

where $\mathbf{0}$ and $\mathbf{I}$ are 4×4 null and identity matrices, respectively. The above equation can be rewritten in the more concise form

$$\Delta\mathbf{u}_\beta = \mathbf{A}(\omega_1 L_1, \omega_2 L_2) \bullet \Delta\mathbf{u}_\alpha \tag{2.13}$$

where the 12×1 vectors $\Delta\mathbf{u}_\alpha$,$\Delta\mathbf{u}_\beta$ and the 12×12 matrix $\mathbf{A}(\omega_1 L_1, \omega_2 L_2)$, which relates $\Delta\mathbf{u}_\beta$ to $\Delta\mathbf{u}_\alpha$, are given in (2.12). Using the definition for $\hat{\varphi}$ in (2.9) and the above introduced grouping of boundary perturbations $\Delta\mathbf{u}_j, j = 1, \ldots 6$ into the two sets $\Delta\mathbf{u}_\alpha$ and $\Delta\mathbf{u}_\beta$, one can rewrite

$$\hat{\varphi} = \begin{bmatrix} \Delta\mathbf{u}_\alpha^* & \Delta\mathbf{u}_\beta^* \end{bmatrix} \begin{bmatrix} \mathbf{K}_{\alpha\alpha}(\lambda) & \mathbf{K}_{\alpha\beta}(\lambda) \\ \mathbf{K}_{\beta\alpha}(\lambda) & \mathbf{K}_{\beta\beta}(\lambda) \end{bmatrix} \begin{bmatrix} \Delta\mathbf{u}_\alpha \\ \Delta\mathbf{u}_\beta \end{bmatrix} \tag{2.14}$$

where the 12×12 submatrices $\mathbf{K}_{\alpha\alpha} = \mathbf{K}_{\alpha\alpha}^T, \mathbf{K}_{\alpha\beta} = \mathbf{K}_{\beta\alpha}^T, \mathbf{K}_{\beta\beta} = \mathbf{K}_{\beta\beta}^T$ are formed by grouping the corresponding $\mathbf{K}_{ij}$'s.

Upon substituting (2.13) into (2.14), the stability problem for the infinite perfect structure reduces to checking the positive definiteness of the following quadratic form

$$\hat{\varphi} = \Delta\mathbf{u}_\alpha^* \bullet \widehat{\mathbf{K}}(\lambda; \omega_1 L_1, \omega_2 L_2) \bullet \Delta\mathbf{u}_\alpha$$
$$\widehat{\mathbf{K}} \equiv \mathbf{K}_{\alpha\alpha} + \mathbf{K}_{\alpha\beta} \bullet \mathbf{A} + \mathbf{A}^* \bullet \mathbf{K}_{\beta\alpha} + \mathbf{A}^* \bullet \mathbf{K}_{\beta\beta} \bullet \mathbf{A} \tag{2.15}$$

where $\mathbf{A}^*$ denotes the adjoint of $\mathbf{A}$ (i.e. the complex conjugate of its transpose). From the symmetry properties of $\mathbf{K}_{\alpha\alpha}$,$\mathbf{K}_{\alpha\beta}$,$\mathbf{K}_{\beta\alpha}$,$\mathbf{K}_{\beta\beta}$ one can verify that the stiffness matrix $\widehat{\mathbf{K}}$ is Hermitian ($\widehat{\mathbf{K}} = \widehat{\mathbf{K}}^*$) and thus has real eigenvalues. This reduces the stability investigation of an infinite, perfectly periodic structure to that of an equivalent but simpler problem involving half the boundary of the unit cell.

The case of a perturbation that has L_I translational symmetry along the X_I direction, i.e. $\omega_I L_I = 0$ for $I = 1$ or 2, admits from (2.12) a rigid body translation in the X_I direction, i.e. $\Delta u_{iI} = \text{const.}$ for $i = 1, \ldots 6$, $I = 1$ or 2. This case is included in the general numerical algorithm described above by imposing, in addition to (2.12) the condition $\Delta u_{1I} = 0$ for $I = 1$ or 2.

The scalar parameter λ is a monotonically increasing "time-like" parameter that characterizes the deformed configuration of the unit cell in the infinite, perfect structure ($\lambda = 0$ corresponds to undeformed, stress-free configuration). If, for a given value of λ, $\widehat{\mathbf{K}}(\lambda; \omega_1 L_1, \omega_2 L_2)$ is positive definite for all dimensionless wavenumbers $(\omega_1 L_1, \omega_2 L_2) \in (0, 2\pi) \times (0, 2\pi)$ the configuration corresponding to λ is stable. Consequently for each pair $(\omega_1 L_1, \omega_2 L_2)$, a minimum load $\lambda_m(\omega_1 L_1, \omega_2 L_2)$ may be found at which $\widehat{\mathbf{K}}$ looses positive definiteness. The critical load λ_c at which the structure first looses stability in a monotonically loading process, is the infimum[7] (i.e. the highest lower bound) of λ_m over the Fourier domain $(0, 2\pi) \times (0, 2\pi)$.

A remark about the nature of the eigenmode corresponding to the critical load λ_c is in order at this point. The surface $\lambda_m(\omega_1 L_1, \omega_2 L_2)$ might exhibit a singular point at the origin $(0,0)$. The physical reason for this singularity is the fact that in the neighborhood of $(0,0)$ one finds, by inspecting (2.12) two different types of modes: (1) the finite wavelength modes for $(\omega_1 L_1, \omega_2 L_2) = (0,0)$ with period one unit cell $\Delta\mathbf{u}(\mathbf{X}) = \mathbf{p}(\mathbf{X})$ and (2) the infinite wavelength modes for $(\omega_1 L_1, \omega_2 L_2) \to (0^+, 0^+)$ that are associated with nearly uniform modes with respect to the unit cell dimensions. When the lowest point of the $\lambda_m(\omega_1 L_1, \omega_2 L_2)$ surface is away from $(0,0)$ the finite wavelength eigenmode requires no special numerical considerations. In the case when the infimum occurs as $(\omega_1 L_1, \omega_2 L_2) \to (0^+, 0^+)$ the critical mode may be a long wavelength one and another numerical technique is needed. Stability is checked in this case by the positive definiteness of the structure's homogenized incremental moduli (for proof see Geymonat et al., 1993). Consequently the structure's stability in the neighborhood of $(\omega_1 L_1, \omega_2 L_2) = (0,0)$ is checked by two different, but complementary calculations.

A final remark: the methodology discussed here pertains to the onset of the first instability at λ_c during the loading of the structure starting at $\lambda = 0$ and is based on calculating $\lambda_m(\omega_1 L_1, \omega_2 L_2)$, the minimum value of λ at which $\widehat{\mathbf{K}}(\lambda; \omega_1 L_1, \omega_2 L_2)$ in (2.15) loses its positive definiteness. In general the structure might regain its stability upon further loading for adequately high values of $\lambda > \lambda_C$. The corresponding critical load λ_C, where stability is regained, can be determined in a similar fashion by finding the supremum (i.e. the lowest upper bound) of $\lambda_M(\omega_1 L_1, \omega_2 L_2)$ over $(0, 2\pi) \times (0, 2\pi)$ where λ_M is the smallest load parameter above which $\widehat{\mathbf{K}}(\lambda; \omega_1 L_1, \omega_2 L_2)$ regains positive definiteness for a given $(\omega_1 L_1, \omega_2 L_2)$.

[7] The concept of infimum is needed in view of a potential singularity at $(0,0)$ of $\lambda_m(\omega_1 L_1, \omega_2 L_2)$, defined in the open domain $(0, 2\pi) \times (0, 2\pi)$. The value of $\lambda_m(\omega_1 L_1, \omega_2 L_2)$ as $(\omega_1 L_1, \omega_2 L_2) \to (0^+, 0^+)$ depends on the ratio $\omega_1 L_1 / \omega_2 L_2$ and one must consider λ_m along all radial paths near $(0,0)$ to find λ_c.

2.3.2. Stability of the finite honeycomb

The stability of the finite structures, perfect or imperfect, is a simpler task that depends on checking the positive definiteness of the entire structure's tangent stiffness matrix $\mathbf{K}(\lambda)$ (see (2.9)). Since this matrix is always available as part of the incremental Newton-Raphson procedure, checking for positive definiteness is a straightforward task that requires the diagonal matrix $\mathbf{D}$ of the $\mathbf{LDU}$ decomposition of $\mathbf{K}$. A matrix $\mathbf{D}$ with all positive diagonal entries corresponds to a stable structure.

3. Numerical approach

The model described in the previous section is employed to predict the response of the SMA honeycomb under a uniaxial compression load–unload cycle along the X_2 direction. This section includes a presentation of selected constitutive parameters, the finite element discretization used, and a description of the numerical algorithm.

3.1. Constitutive parameters

Three different types of uniaxial constitutive laws are used in this study: a symmetric tension–compression law (Model 1), a more realistic asymmetric law to capture the behavior of textured polycrystals (Model 2), and a model calibrated to a specific honeycomb experiment (Model 3). Table 1 provides specific parameters used as base cases for the parameter study that follows. When studying the influence of a specific parameter on the SMA honeycomb response, the values of the parameter that are different from the base case value appearing in the table will be indicated on the corresponding response curve.

3.2. Finite element discretization and numerical algorithm

The numerical algorithm employed in the subsequent calculations is based on the finite element method (FEM) and the discretization of the 1-D beam model given in Eqs. 2.1, 2.2 and 2.3. Our FEM model was implemented in the research software framework, FEAP (2005). The approach is a fairly standard incremental procedure; however, a few relevant details are presented here.

Each cell wall was divided into 20 elements of equal length, except for the calculations for the special case $E_t = 0$ which required 160 equal length elements to capture the concentration of curvature near the two ends of each deforming ligament. Within each element, a Hermitian cubic interpolation was used for the displacements $v(x), w(x)$, resulting in four degrees of freedom (DOFs) per node, i.e. $v(x_n)$, $v_{,x}(x_n)$, $w(x_n)$, $w_{,x}(x_n)$. A four point Gauss quadrature was used for numerical integrations in the x-direction of each element. When the principal solution under monotonic loading was of interest, the through the thickness integrations were computed analytically (e.g. Figs. 3–5). In subsequent cases when hysteretic solutions were calculated, a 51-point trapezoidal rule with equidistant points was used for thickness integrations in the y-direction. This rather large number of points in the y direction was required to capture the evolution and precise locations of phase mixture boundaries.

The elements' translational degrees of freedom v and w must be transformed to the global coordinate system to enforce displacement continuity at the junction nodes. It can be shown that the

Table 1
Constitutive models.

	Model 1	Model 2	Model 3
$E_A = E_M^+ = E_M^-$	1	1	75 GPa
E_l^+	0.05	0.05	11.25 GPa
E_u^+	0.05	0.05	10.3646 GPa
E_l^-	0.05	0.15	15 GPa
E_u^-	0.05	0.15	16.2766 GPa
β^+	0.0418	0.0418	0.031025
β^-	−0.0418	−0.02125	−0.0184
ε_n^+	0.006	0.006	0.0035
ε_n^-	−0.006	−0.012	−0.007
$\Delta\sigma_A^+$	0.002	0.002	0.1875 GPa
$\Delta\sigma_A^-$	0.002	0.002	0.2625 GPa

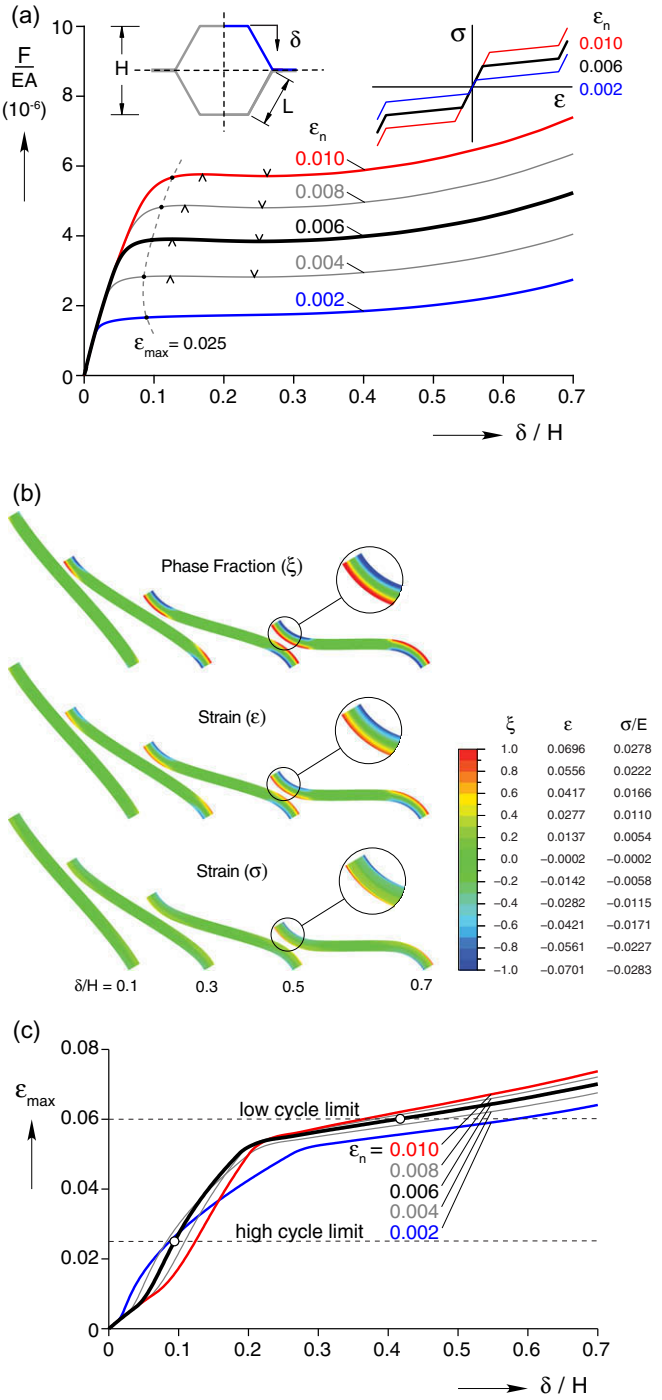

Fig. 3. (a) Principal branches of the dimensionless macroscopic compressive stress (F/EA) vs. compressive strain (δ/H) response of the infinite-perfect honeycomb, based on constitutive Model 1 (right inset), showing the influence of nucleation strain (ε_n). (b) Contours of phase fraction (ξ), local strain (ε), and local stress (σ/E) in the slanted cell wall (Model 1, $\varepsilon_n = 0.006$). (c) Maximum local tensile strain (ε_{max}) as a function of macroscopic compression (δ/H) for the same constitutive laws of 3(a).

rotation angle ψ satisfies (in local coordinates) $\tan\psi = w_{,x}/(1 + v_{,x})$. Of the several choices that one can impose rotation continuity between adjacent elements at the junction nodes (three kinematic conditions but four DOFs available) the simplest one is by imposing continuity of the local derivatives ($v_{,x}$ and $w_{,x}$), treating these now as global DOFs, since they still maintain rotary continuity between adjacent beam elements (see again Triantafyllidis and Schraad, 1998).

An incremental Newton–Raphson procedure was employed to solve the resulting equations. In all but the final experiment simulations top and bottom displacement boundary conditions were enforced directly (by reduction of the equilibrium equations) while lateral edges were unconstrained. For the final simulations of the actual honeycomb structure a penalty-based contact algorithm with regularized Coulomb friction was used to capture nonuniform contact and frictional effects of the platens. The loading increment was approximately 0.14% macroscopic strain for the infinite structures stability calculations, while it was occasionally lowered to help the convergence of the finite sized structures.

4. Results and discussion

The results of several FEM simulations are now presented, progressing from the infinite-perfect honeycomb to the finite-perfect honeycomb and then to the finite-imperfect honeycomb. We proceed incrementally, starting with the infinite-perfect structure, since the principal path configurations are simple, periodic ones and the analysis gives one a sense of the "bulk" (many cell) behavior independent of boundary issues. It is a convenient context to perform a parameter study of the material law. The finite-perfect structure cases help to address the added influence of boundary constraints on the behavior, and the finite-imperfect structure cases helps to quantify the imperfection sensitivity of the response. Stability issues and the influence of constitutive parameters are discussed for each case. The monotonically increasing loading parameter λ of Section 2.3 is taken to be δ/H for loading phase ($\dot{\delta} > 0$) and $2(\delta/H)_{max} - \delta/H$ for unloading ($\dot{\delta} < 0$) where δ/H is the macroscopic strain.

4.1. Principal branch of the infinite, perfect honeycomb

We studied the influence of constitutive parameters on the response of the infinite-perfect honeycomb as shown in Figs. 3–8, where at this point, all deformations were assumed to be cell-periodic. Results are plotted in diagrams of compressive, dimensionless macroscopic stress F/EA vs. macroscopic strain δ/H. The cross-sectional area, A, was taken as the total inclusive reference (initial) area of the footprint of the envelope of the honeycomb, to obtain an average-homogenized stress measure. The influence of material parameters associated with the loading part of the constitutive law, i.e. ε_n and E_t, is presented in Figs. 3–5, while the influence of the hysteretic part of the constitutive law is investigated in Figs. 6–8. Since all cells deform identically (cell-periodic) in the principal solution of the infinite-perfect structure, due to the symmetry of geometry and loading, only a quarter of the unit cell, shown as an insert in these figures, was required in the calculations. In fact, only the slanted ligament was needed, since the horizontal cell walls remained unstressed. The different uniaxial constitutive laws used are shown as inserts in the corresponding figures.

The influence of the nucleation strain ε_n on the principal solution under loading, for the case of a symmetric (tension–compression) uniaxial response, is shown in Fig. 3(a). As expected, increasing $\varepsilon_n^+ = \varepsilon_n^-$ from 0.002 to 0.010 (centered on the base case of Model 1, $\varepsilon_n = 0.006$) results in delaying the deviation of the structure's response away from the initial, nearly linear regime. Moreover, while increasing ε_n raises the stress at the onset of the $A \rightarrow M$ transformation, it softens the initial tangent modulus (plateau regime, near $0.1 < \delta/H < 0.4$). The responses then stiffen at larger macroscopic strains ($\delta/H > 0.5$). Limit loads, both local maxima and minima, are shown by $\wedge$ and $\vee$, respectively, in the figure. Note that no such limit load exists for the lowest value of $\varepsilon_n = 0.002$. Points are also shown where the local maximum tensile strain has reached 0.025, a commonly imposed limit for high cycle fatigue life of Nitinol. This shows the "strain amplification" achieved by the thin walled honeycomb, since it occurs at macroscopic strains near 0.1. The initial softening of the response is due to a geometric effect of the deforming cell walls which results in the appearance, above a certain value of ε_n, of a local maximum in the macroscopic stress–strain response, despite the fact that the underlying constitutive response of the material is strictly stable, i.e. $E > E_t > 0$.

Fig. 3(b) shows contours of phase fraction (ξ), local strain (ε), and normalized local stress (σ/E) in the slanted cell wall at four values of compressive strain (δ/H). It shows that transformation is concentrated at the ends of the ligament, especially in the corners. The phase fraction and strain have nearly linear distributions across the thickness, but the stress has a nonlinear distribution, as one would expect from the constitutive law. We recognize that the maximum stress at the largest macroscopic compressive strain shown ($\delta/H = 0.7$) is unrealistically large (near 2 GPa for a typical value of $E = 75$ GPa), indicating that local plasticity and significant "locked-in" martensite (not modeled here) would actually exist at such large macroscopic strains, thereby preventing perfect superelasticity upon unloading.

The usual figures-of-merit for honeycombs made of conventional metals are specific stiffness and energy absorption capability, but the use of SMAs now allows us to additionally consider the more ambitious goal of recovering the macroscopic strain after significant deformation. One should, therefore, consider the material's strain recovery limitations to ensure macroscopic strain recovery can actually be realized. Fig. 3(c) plots the maximum local tensile strain ($\varepsilon_{\max}$), i.e., worst case of all (x,y) points in the structure, as a function of macroscopic compressive strain (δ/H) for the various parameters of ε_n. With relatively large values of ε_n the maximum local strain is roughly tri-linear. For the base case of Model 1 ($\varepsilon_n = 0.006$), the maximum local strain grows linearly until about $\delta/H = 0.05$, then grows more steeply until about $\delta/H = 0.18$, and then levels off at a lower slope. At a maximum local strain of 0.025 (approximate high cycle strain limit for NiTi) the corresponding macroscopic strain is about 0.094. At a maximum local strain of 0.06 (a reasonable local strain limit for low cycle operation) the corresponding macroscopic strain is about 0.417, giving a sense of the strain amplification of the honeycomb structure. Thus, Fig. 3(c) provides guidelines for the range of macroscopic (global) strains that can be accommodated by local martensitic transformation in the SMA material without incurring significant plasticity that would otherwise impede reverse transformation upon unloading.

Fig. 3(c) also shows the advantage of an SMA over a conventional metallic (e.g. aluminum) honeycomb. Since the yield strain for aluminum is typically of the order of 0.002, the maximum reversible macroscopic strain (elastic range) for an aluminum honeycomb would be, according to Fig. 3(c), less than $\delta/H = 0.02$, over 20 times lower than the corresponding value for an SMA honeycomb of the same geometry ($\delta/H = 0.417$). Alternatively, one could reduce the t/L ratio to keep the conventional honeycomb within its elastic range, but as noted in Shaw et al. (2007b) this would sacrifice stiffness by a factor of over 1000, since the stiffness of the honeycomb scales roughly by $(t/L)^3$, thereby making this an impractical prospect.

The influence of the transformation tangent modulus E_t on the perfect structure's principal loading solution, for the symmetric uniaxial response is presented in Fig. 4. As expected, increasing E_t/E stiffens uniformly the $A \rightarrow M$ transformation regime. However, it is worth noticing that for $E_t/E = 0$ a maximum exists in the macroscopic stress–strain response soon after the structure deviates from its linear regime. The load maximum persists even for the case of the strictly monotonic uniaxial response at $E_t/E = 0.05$, albeit at a larger macroscopic strain. Upon further increase to $E_t/E = 0.1$ the macroscopic stress–strain response is monotonic (no limit loads), thus implying that the constitutive stiffening overcomes the geometric softening effect. We should mention here that, not surprisingly, numerical difficulties were encountered for the case of $E_t/E = 0$. The deformed shape of the cell involved extreme bending localization at the ends of the slanted wall. The cell wall's curvature experienced a sharp change, which required a higher number of elements (160 elements along the cell wall length).

The influence of the tensile transformation tangent modulus E_t^+ on the infinite-perfect structure's principal solution under loading, but for the asymmetric constitutive law (Model 2), is presented in Fig. 5. The material's stiffer response in compression ($E_t^-/E = 0.15$), as compared to tension, resulted in about 25% higher macroscopic stresses for a given macroscopic strain than occurs for the its symmetric counterpart in Fig. 4. Since the bending of cell walls involves compressive as well as tensile stresses, the higher stiffness of the compressive transformation zone ($E_t^-/E > E_t^+/E$) as well as its smaller transformation strain ($\beta^- > \beta^+$) resulted in a higher macroscopic tangent moduli for a given macroscopic strain as seen in Fig. 5 compared to Fig. 4. Notice that the structure's macroscopic stress–strain response shows a limit load only for $E_t^+/E = 0$, but weaker than in Fig. 4.

The influence of the amplitude of the hysteresis loop $\Delta\sigma$ for a symmetric uniaxial material law is presented in Fig. 6, where unloading for all cases start at macroscopic strains $\delta/H = 0.3$, 0.5 and 0.7. Notice that the initial slope of the unloading branch decreases as the macroscopic strain at unloading increases, due to the resulting geometric change of the unit cell. Also notice that for the smallest amplitude of hysteresis $\Delta\sigma/E = 0.002$ the unloading branch starting from the lower strains $\delta/H = 0.3$ and $\delta/H = 0.5$ converge rapidly to the corresponding unloading branch that starts at $\delta/H = 0.7$. As $\Delta\sigma$ increases, the discrepancies between the different unloading paths progressively increase. Also, hysteresis values greater than 0.003 eliminate any possibility of limit loads in the unloading curves.

The influence of the tensile transformation tangent modulus E_t^+, but for the asymmetric constitutive law (Model 2), is presented in Fig. 7, where as in Fig. 6, unloadings at $\delta/H = 0.3$, 0.5 and 0.7 were considered. As expected from the results of Fig. 5, an increase in E_t^+/E results in an overall stiffer response, occurring at progressively higher macroscopic stress levels (for the same macroscopic strains). Notice that, similar to Fig. 6, the initial slope of the unloading branch decreases with increasing strain at unloading but is independent of E_t^+, i.e. unloading branches starting at the same macroscopic strain are approximately initially parallel to each other, since the deformed geometries are comparable at this point.

A noteworthy feature of the results presented in Fig. 6 is the near independence of the unloading branch on the structure's deformation history, since all three unloading branches converge to the same curve, after some initial elastic unloading. To further illustrate the near load-path independence of the principal solution's unloading branch, Fig. 8 compares, for the symmetric constitutive law, the unloading paths obtained by reversing the macroscopic strain at $\delta/H = 0.3$, 0.5 and 0.7 to the loading path of the same structure with an "elastic" constitutive response that coincides with the unloading branch of the hysteretic model (see

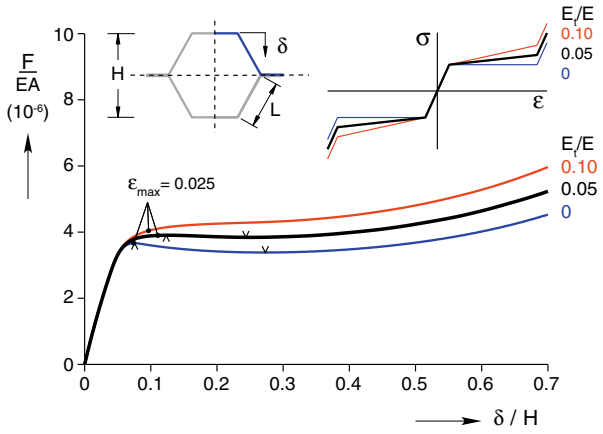

Fig. 4. Principal branches of the dimensionless macroscopic compressive stress (F/EA) vs. compressive strain (δ/H) response of the infinite-perfect honeycomb, based on constitutive Model 1 (right inset), showing the influence of transformation tangent modulus (E_t).

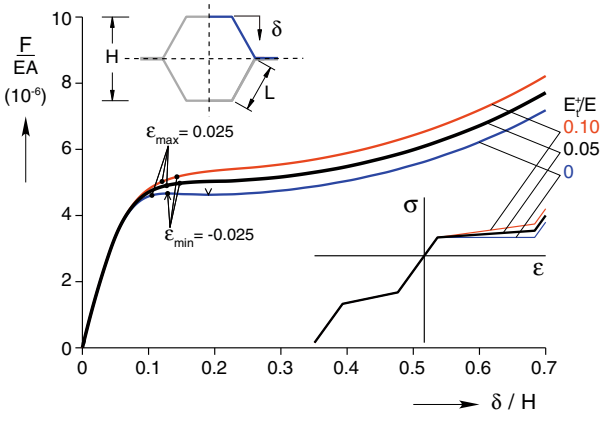

Fig. 5. Principal branches of the dimensionless macroscopic compressive stress (F/EA) vs. compressive strain (δ/H) response of the infinite-perfect honeycomb, based on asymmetric constitutive Model 2 (right inset), showing the influence of tensile transformation tangent modulus (E_t^+).

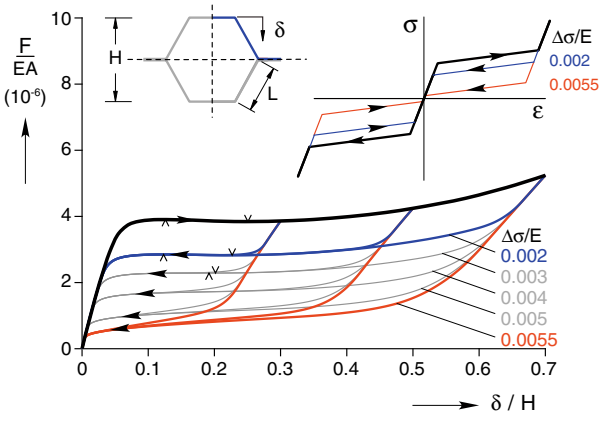

Fig. 6. Principal branches of the dimensionless macroscopic compressive stress (F/EA) vs. compressive strain (δ/H) load–unload responses of the infinite-perfect honeycomb, based on hysteretic constitutive Model 1 (right inset), showing the influence of stress hysteresis ($\Delta\sigma/E$). Unloading paths shown start at macroscopic strains $\delta/H = 0.3$, 0.5, 0.7.

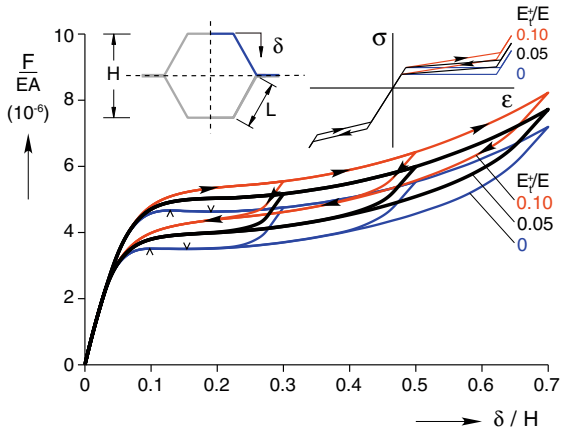

Fig. 7. Principal branches of the dimensionless macroscopic compressive stress (F/EA) vs. compressive strain (δ/H) load–unload responses of the infinite-perfect honeycomb, based on asymmetric, hysteretic constitutive Model 2 (right inset), showing the influence of tensile transformation modulus (E_t^+).

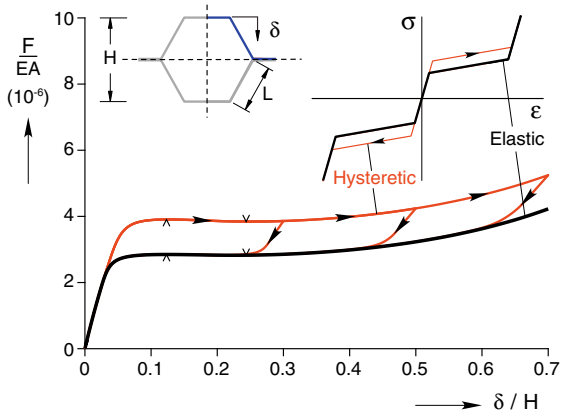

Fig. 8. Principal branches of the dimensionless macroscopic compressive stress (F/EA) vs. compressive strain (δ/H) response of the infinite-perfect honeycomb, based on constitutive Model 1 (right inset), comparing the unloading response of the hysteretic model with an "elastic" one.

insert of Fig. 8). The comparison indeed confirms that the response during active $A \leftrightarrow M$ transformation is nearly independent of the loading path, i.e. the response eventually tends towards a fundamental "outer-loop" response, consistent with the chosen material law.

4.2. Stability of the infinite, perfect honeycomb

The next set of calculations, presented in Figs. 9–14 address the stability of the principal solution of the infinite-perfect structure under displacement (δ/H) control (stiff loading device) for the same constitutive laws used previously in Figs. 3–8. The full unit cell (shown as an insert in these figures) was now required to perform the Bloch wave stability calculations. Stable equilibrium paths are indicated with a bold line, while unstable paths are drawn with a thin line. Limits loads are indicated as before with $\wedge$ and $\vee$. Critical points, where the stability of the path changes, are shown with open circles.

The stability of the loading path of the principal (unit cell-periodic) solution of the infinite-perfect structure for a symmetric constitutive response, but with different nucleation strains ε_n, is

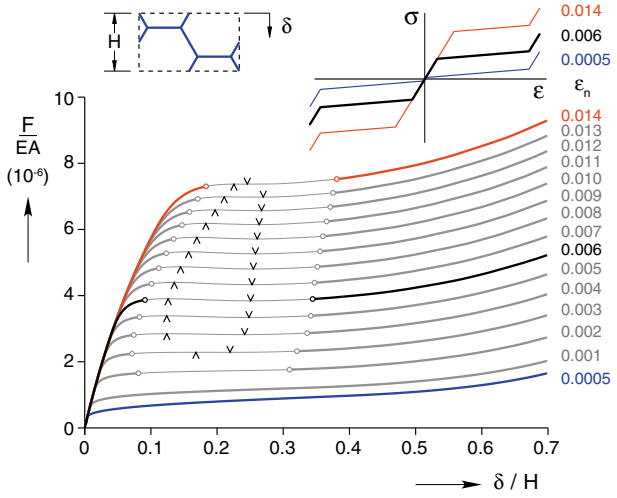

Fig. 9. Stability of macroscopic compressive stress–strain, (F/EA) vs. (δ/H), responses for the perfect, infinite honeycomb under δ/H control, showing the influence of nucleation strain (ε_n). Stable and unstable segments are indicated by thick and thin lines, respectively, and stability changes are shown with circles on the paths.

shown in Fig. 9. Notice that for sufficiently low $\varepsilon_n \leqslant 0.001$, the principal solution is stable for all strains. Interestingly, the case of $\varepsilon_n = 0.002$ has critical bifurcation points, yet no limit loads. As ε_n increases further, and the corresponding macroscopic tangent modulus softens, an unstable zone appears. At sufficiently large strains, however, it restabilizes as transformation saturates and the increased material stiffness overwhelms the kinematic softening of the cell. Additionally, note that in each case for $\varepsilon_n \geqslant 0.003$ the onset of instability precedes the maximum load, i.e., while the response still has a positive slope, and then the path regains stability after the local minimum. The presence of an unstable region in the principal solution of the infinite-perfect structure has important implications for the behavior of finite structures, perfect and imperfect, as will be seen subsequently.

Some comments are in order about the nature of the critical modes at the two end points of the unstable zones, i.e., at the first onset of instability and termination of instability along the principal path. In both cases the critical mode is a long wavelength mode. Fig. 10 presents an analysis for the case of Model 1 (base case of Fig. 9), showing the critical macroscopic strain as a function of dimensionless wavenumbers $(\omega_1 L_1, \omega_2 L_2)$, i.e surface $\lambda_m(\omega_1 L_1, \omega_2 L_2)$ corresponding to the first loss of positive definiteness of $\hat{\mathbf{K}}$ as defined in Section 2.3.1. The onset of instability occurs at $\delta/H = 0.092$ with the minimum load corresponding to wavenumbers near the origin, indicating a possible long wave length mode. The origin $(\omega_1 L_1, \omega_2 L_2) \to (0,0)$ is a singularity of the Bloch wave analysis, so the critical mode shown here does not quite reach the origin due to the discretization of wave numbers used. Consequently, the long wave length mode was confirmed by a separate analysis of the homogenized moduli. A similar situation occurs at the termination of the unstable range at $\delta/H = 0.342$, where the instability mode is again a long wavelength one. At intermediate strains the path is unstable, as shown in Fig. 9.

These characteristics are typical of the instability of the principal load path in all cases considered in this paper. The fact that the eigenmode corresponding to λ_c is a "global", i.e. long wavelength mode, and not a "local" one is due to the particular loading orientation and is perhaps not surprising in view of results by Triantafyllidis and Schraad (1998) (same geometry, similar bilinear constitutive law). Other load orientations would likely exhibit instability with respect to modes of finite wavelength. Indeed, in

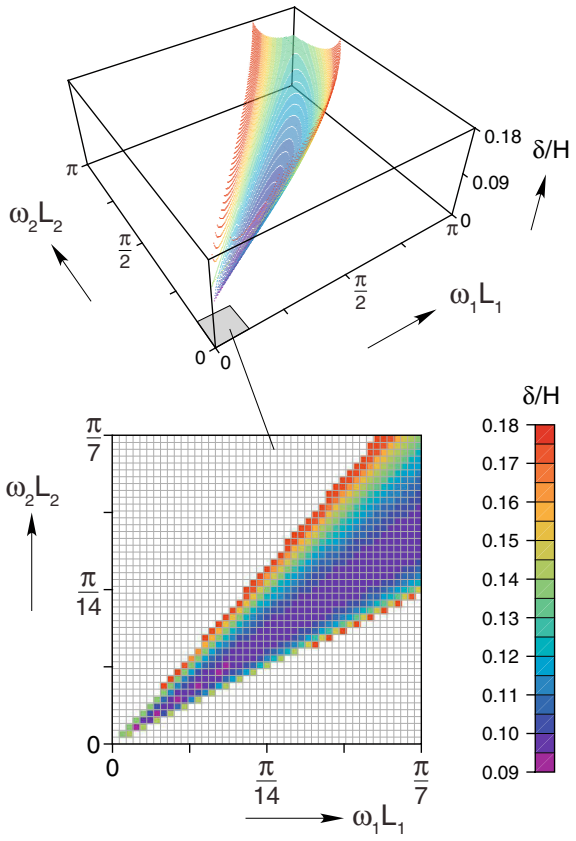

Fig. 10. Lowest strain (δ/H) as a function of dimensionless wave numbers $(\omega_1 L_1, \omega_2 L_2)$ on the onset of instability of the infinite-perfect honeycomb calculated along the principal path with a symmetric, "elastic" constitutive law (Model 1). The minimum $(\delta/H = 0.092)$ occurs as $(\omega_1 L_1, \omega_2 L_2) \to (0,0)$, indicating a long wavelength critical mode, which is confirmed from a loss of ellipticity calculation of the homogenized incremental moduli.

a series of in–plane crushing experiments of Aluminum honeycomb, Papka and Kyriakides (1994) compressed the structure along the X_1 direction and found that the corresponding critical mode is a "local" one, a fact that was verified subsequently by the Bloch wave analysis of Triantafyllidis and Schraad (1998).

The influence of the tangent modulus E_t for the symmetric constitutive law (Model 1) on the stability of the loading path of the principal solution of the infinite-perfect structure is shown in Fig. 11. As expected, increasing E_t/E results in decreasing the extent of the unstable zone. As seen before, for cases $E_t/E = 0{,}0.05$ the extent of instability extends beyond the range of negative slope in the principal path (between limit loads). Even for the case $(E_t/E = 0.10)$, where the path maintains a positive slope, a significant regime of instability exists. Despite the risk of belaboring a (perhaps) obvious point, we wish to emphasize here that monotonicity of the principal path is clearly not a sufficient criterion for stability.

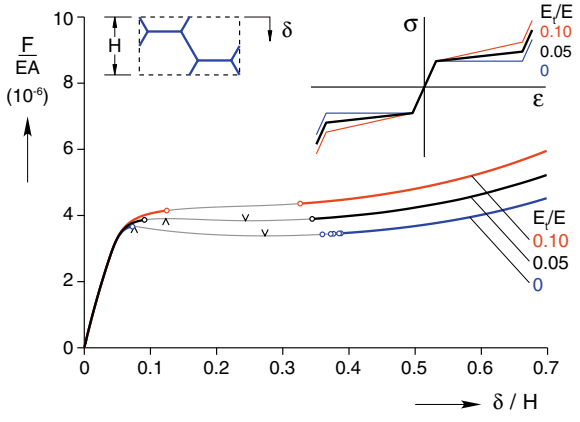

Fig. 11. Stability of macroscopic compressive stress–strain, (F/EA) vs. (δ/H), responses for the perfect, infinite honeycomb under δ/H control, showing the influence of transformation modulus (E_t) using Model 1 as the base case. Note, multiple changes in stability occur along the response for $E_t = 0$.

The results in Fig. 12 demonstrate the stability of the principal solution for the infinite-perfect structure, but for the asymmetric constitutive response (Model 2). As expected from the stiffer response of the material in compression, the extent of the unstable zones is considerably smaller compared to corresponding results in Fig. 11 for the same E_t^+/E.

The stability for both the loading and the unloading branches of the principal solution of the infinite perfect structure is presented for the symmetric and asymmetric hysteretic constitutive laws, respectively, in Figs. 13 and 14. The influence of hysteresis $\Delta\sigma/E$ (same range as in Fig. 6) on the stability of the loading–unloading path (using the symmetric Model 1) is presented in Fig. 13. Except for the highest value $\Delta\sigma/E = 0.0055$, instability regions exist in both the loading and unloading paths. Fig. 14 shows the influence of E_t^+/E on the stability of the principal solution of the infinite perfect structure having the same hysteretic, asymmetric constitutive laws (based on Model 2) as in Fig. 7. In this case only the loading

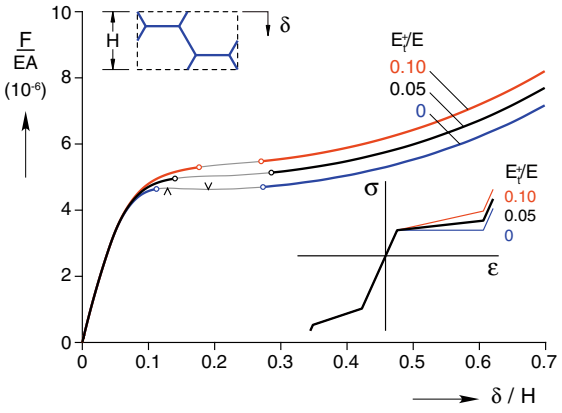

Fig. 12. Stability of macroscopic compressive stress–strain, (F/EA) vs. (δ/H), responses for the perfect, infinite honeycomb under δ/H control based on asymmetric Model 2, showing the influence of tensile transformation modulus (E_t^+).

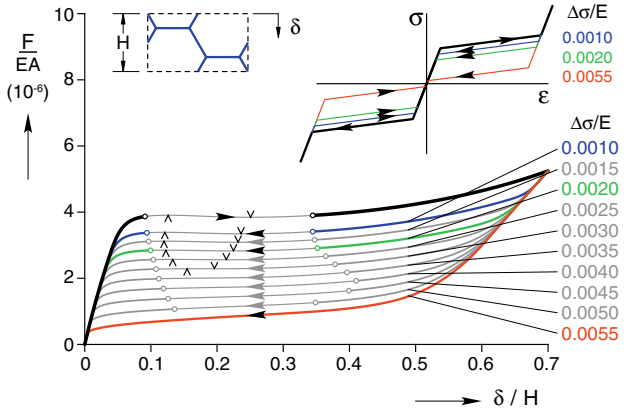

Fig. 13. Stability of macroscopic compressive stress–strain, (F/EA) vs. (δ/H), load–unload responses for the perfect, infinite honeycomb under δ/H control, showing the influence of stress hysteresis $(\Delta\sigma/E)$ for symmetric, hysteretic material.

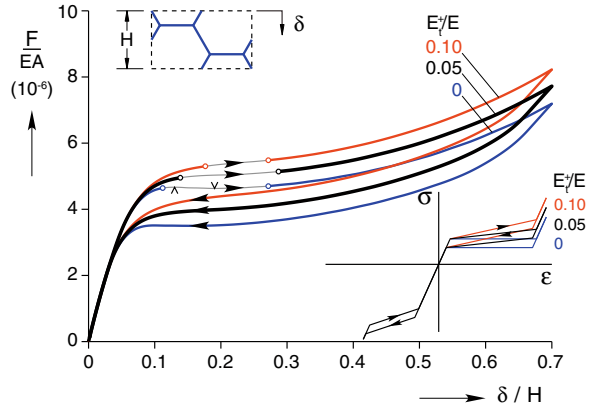

Fig. 14. Stability of macroscopic compressive stress–strain, (F/EA) vs. (δ/H), load–unload responses for the perfect, infinite honeycomb under δ/H control, showing the influence of tensile transformation modulus (E_t^+) for asymmetric, hysteretic material (based on Model 2).

paths have unstable regions, while all the unloading paths shown are stable, even for the case where $E_t^+/E = 0$.

4.3. Response of the finite, perfect honeycomb

Finite element simulations of perfect honeycombs of finite size are presented in Figs. 15 and 16 to investigate the influence of boundary conditions. The selected geometry corresponds to the topology (but with an idealized, perfect geometry) and overall dimensions of the fabricated specimen used in the isothermal experiment of Shaw et al. (2007b), to be presented later in Section 4.5.

The response of the finite size, perfect structure under uniaxial compression calculated for a symmetric, hysteretic constitutive law (Model 1) is presented in Fig. 15. The loading device was modeled as frictionless. The principal solution of the finite, perfect structure has all cells deforming identically and hence coincides with the principal solution of the infinite perfect structure (yet the stress-free lateral edges may have new implications for stability). For comparison the response of the principal solution for the infinite-perfect structure is also shown in the same figure. The macroscopic force–displacement loading–unloading curves for both (infinite and finite) structures are given in Fig. 15a. The infinite honeycomb response has unstable segments during loading and unloading, yet the finite honeycomb response does not. The responses of the two structures are similar, but start diverging on the loading and unloading branches near the onset of instability of the infinite structure. It is not surprising that the responses of the finite-perfect and infinite-periodic structures coincide again at macroscopic strains well above or below the strain levels where the paths of the infinite-periodic solution are stable.

A better, quantitative measure of the deviation between the finite and infinite honeycomb solutions is shown in Fig. 15b. The relative L_2 norm of the two solutions, $\|\mathbf{u}-\mathbf{u}_\#\|/\|\mathbf{u}_\#\|$, is plotted against the macroscopic strain, where

$$\|\mathbf{u}_\#\|^2 \equiv \int_{\text{cellwalls}} \left[v_\#^2(x) + w_\#^2(x)\right] dx,$$
$$\|\mathbf{u}-\mathbf{u}_\#\|^2 \equiv \int_{\text{cellwalls}} \left[(v(x)-v_\#(x))^2 + (w(x)-w_\#(x))^2\right] dx, \quad (4.1)$$

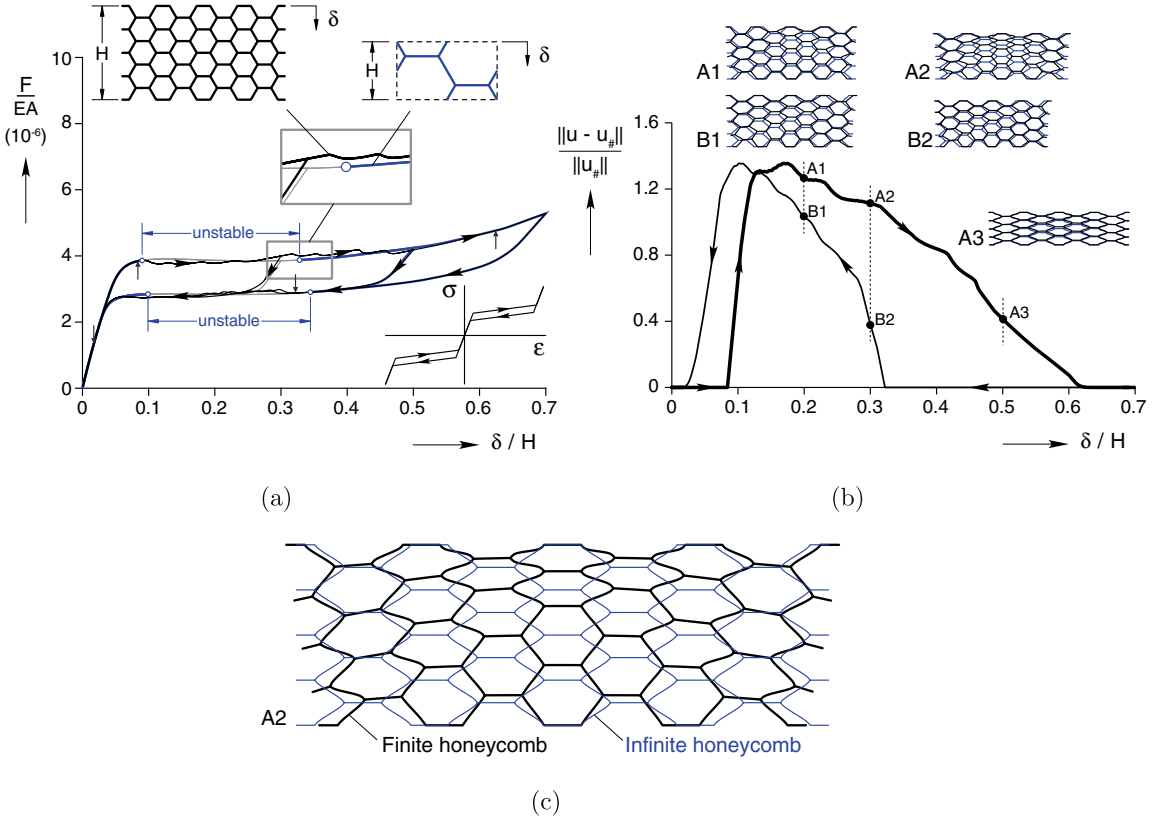

Fig. 15. (a) Comparison of compressive loading–unloading responses of the finite (upper left inset) and infinite (upper right inset) perfect honeycombs with a symmetric, hysteretic constitutive response (Model 1). (b) Relative deviation $\|\mathbf{u}-\mathbf{u}_\#\|/\|\mathbf{u}_\#\|$ of the finite honeycomb's deformation $(\mathbf{u})$ from the infinite honeycomb's principal path deformation $(\mathbf{u}_\#)$ vs. macroscopic compressive strain (δ/H). The finite and periodic configurations are shown in insets at strains 0.2, 0.3 and 0.5 (loading path configurations A1, A2, A3 and the unloading path configurations B1 and B2.) (c) Magnified view of configuration A2 for the finite and infinite (periodic) configurations.

and (v,w) and $(v_{\#},w_{\#})$ are the respective displacements of the finite and infinite (periodic) honeycombs. The integrals over the cell walls are calculated numerically using the same Gaussian quadrature used in the equilibrium calculations.

The deviation of the finite honeycomb's equilibrium path in Fig. 15b from its periodic counterpart during loading occurs at $\delta/H = 0.084$, (denoted by ↑ in Fig. 15a) which just precedes the first instability at $\delta/H = 0.092$ encountered of the infinite structure.[8] The deviation disappears near $\delta/H = 0.624$ well after the final bifurcation point at $\delta/H = 0.328$. Upon unloading, deviation between the two paths appears at $\delta/H = 0.322$ soon after the bifurcation point at $\delta/H = 0.344$ and then disappears at $\delta/H = 0.018$ well after the final bifurcation point at $\delta/H = 0.099$.

The deformed configurations of the finite and infinite honeycombs are shown in Fig. 15b at five different states: points A1, A2 and A3 on the loading branch ($\delta/H = 0.20, 0.30, 0.5$) and points B2 and B1 ($\delta/H = 0.30, 0.20$) on the unloading branch. The numerical calculations for the hysteretic, finite sample were obtained by a straightforward incremental algorithm with small step sizes (typically $\Delta\delta/H$ between about 3×10^{-5} and 9×10^{-5}). This standard procedure, without any special modification, was adequate to allow the finite structure to take a particular, non-periodic, equilibrium path. As can be seen in the magnified view of state A2 in Fig. 15c the overall shape of the finite honeycomb takes a roughly trapezoid shape, with cells flattening at the top more than at the bottom. Of course, other equilibrium paths exist, which are symmetry related to the calculated equilibrium path. The presence of internal variables in the model introduces numerical imperfections, thus selecting one of the geometrically equivalent paths. Other equilibrium paths are likely to exist (after all, the periodic solution has a high number of symmetries), but the ease with which numerical solutions were found (without any overt imperfections included) leads us to believe, although without proof at this time, that the numerical solution found here is the energetically preferred path in a continuous loading process of the structure. Furthermore, the deformed patterns obtained are reminiscent of the configurations observed in experiments (Shaw et al., 2007b).

The mechanical response of the finite honeycomb using the asymmetric constitutive response (Model 2) is presented in Fig. 16. For comparison purposes the results are overlaid on the stability results for the corresponding infinite periodic case (from Fig. 14). As before the finite honeycomb's force–displacement curve deviates from its periodic counterpart near the onset of first instability. However, a deviation of the finite size structure's response from the corresponding periodic results is found on the unloading path as well. This discrepancy is unexpected, in view of the stability of the entire unloading path of the infinite, periodic solution found according to the results in Fig. 14. However, this mystery can be explained by the presence of the tiny unstable region on the principal unloading branch of the finite structure (In fact, this unstable region was not initially detected until a more detailed calculation was performed with very fine increments). Interestingly, the infinite honeycomb response has an unstable segment during loading but not unloading, yet the finite honeycomb response is stable during loading but has this short unstable segment during unloading.

4.4. Response of finite, imperfect honeycombs

The influence of imperfections on the response of the actual, finite size structure is shown in Figs. 17 and 18 for the symmetric and asymmetric constitutive response, respectively. The construction of a "hypothetical" imperfect structure was achieved by randomly perturbing the location of the internal cell junctions of the perfect structure. Each node of the perfect specimen was displaced within a disc of radius $\Delta r = \zeta L$ (where L is the unit cell side), where the radius and the angle for the nodal perturbation vector were chosen randomly in the respective intervals $[0, \Delta r)$ and $[0, 2\pi)$.

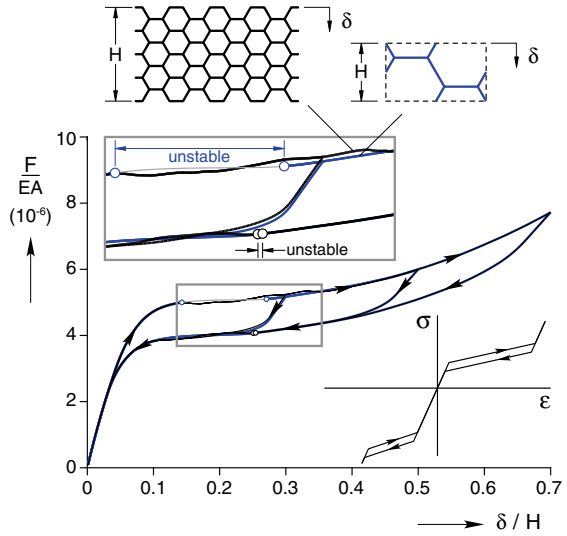

Fig. 16. Comparison of compressive loading–unloading responses for the finite (upper left inset) and infinite (upper right inset) perfect honeycombs with an asymmetric, hysteretic constitutive response (Model 2).

Fig. 17(a) shows the macroscopic stress–strain responses of the perfect ($\zeta = 0$) and two imperfect ($\zeta = 0.01, 0.1$) structures. The paths are similar, undulating about a plateau stress at intermediate strains, yet all the paths shown are stable everywhere. The figure reveals little influence of the imperfection for the small imperfection amplitude ($\zeta = 0.01$) but more significant deviations from the perfect responses for the larger amplitude ($\zeta = 0.1$), especially at large strains ($\delta/H > 0.5$). The same conclusion can be reached from Fig. 17(b), where the relative deviation between the finite and periodic solution is plotted as a function of macroscopic strain. As expected, the loading–unloading curve for the smaller imperfection ($\zeta = 0.01$) is closer to the perfect case ($\zeta = 0$) than the corresponding curve for the larger imperfection ($\zeta = 0.1$). Fig. 17(b) shows that the configurations diverge from each other at small macroscopic strains initially (say, $\delta/H < 0.05$), but then tend to converge somewhat toward the perfect case as strains near $\delta/H = 0.1$. The largest differences between the three cases are apparent in Fig. 17(b) upon unloading (from $\delta/H = 0.7$ down to about $\delta/H = 0.2$), but then they converge closely to the perfect case at small strains ($\delta/H < 0.1$).

The comparison of the macroscopic stress–strain response of the finite, perfect ($\zeta = 0$) and two imperfect ($\zeta = 0.01, 0.1$) structures for the case of the asymmetric constitutive law (Model 2) is presented in Fig. 18. Again, all paths shown are stable everywhere, showing that while the path undulates for much of the path, imperfections help to suppress the possibility of instability. Consistent with the results of Fig. 17, there is little difference between the behavior of the perfect ($\zeta = 0$) and the slightly imperfect ($\zeta = 0.01$) structures, and a more apparent difference with the more imperfect structure ($\zeta = 0.1$).

4.5. Response of the fabricated nitinol honeycomb

Finally, we turn to superelastic simulations of an actual SMA honeycomb. All the above presented results pertain to various idealized SMA structures. The following results are calculated for the actual SMA honeycomb specimen shown in Fig. 19(a), having over-

[8] Instability of the finite-perfect structure precedes the onset of instability of the infinite counterpart, since it is not laterally constrained.

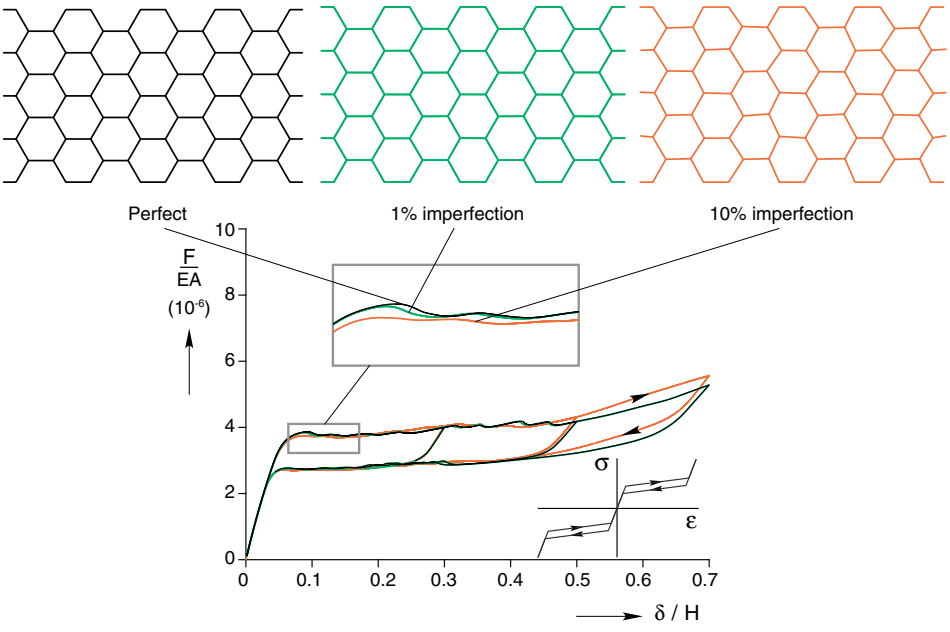

(a)

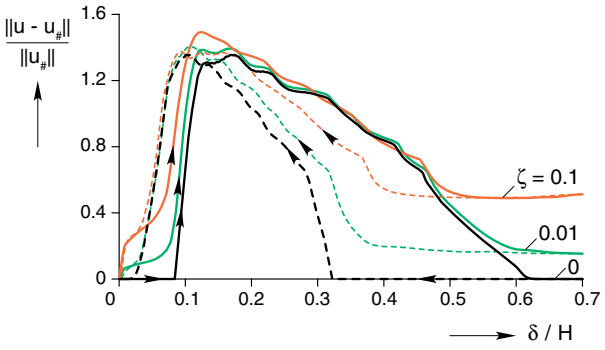

(b)

Fig. 17. (a) Comparison of compressive loading–unloading responses for finite perfect and imperfect honeycombs ($\zeta = 0, 0.01, 0.1$) with a symmetric, hysteretic constitutive response (Model 1). (b) Relative deviation $\|\mathbf{u} - \mathbf{u}_{\#}\|/\|\mathbf{u}_{\#}\|$ of the finite perfect and imperfect honeycomb deformations vs. macroscopic compressive strain (δ/H).

all in-plane dimensions 40.6 × 21.5 mm with 4-1/2 ×7 cells, out-of-plane depth *5.2* mm, and nominal ligament thickness $t = 0.1$ mm, except for the double layer bonds at the horizontal lands. The uniaxial macroscopic stress–strain response to several compressive load cycles is shown in Fig. 19(b) (data redrawn from Fig. 5 of Shaw et al. (2007b)). The actual geometry of the specimen in Fig. 19(a) was digitized as accurately as possible and was discretized by up to 20 beam elements per ligament. The cell ligaments of the SMA honeycomb specimen are noticeably curved, especially at the junctions, thus requiring more finite elements to accurately capture the initial geometry.

The local stress–strain behavior of the as-fabricated honeycomb walls is, unfortunately, not directly available at this time, and this would be challenging task to obtain for a number of reasons. The post heat-treated properties are likely different from the virgin NiTi strip material used in their construction, so one would want properties of wall samples excised from the honeycomb. One could only hope to get tensile data, not compression data, since buckling would be difficult to avoid. Obtaining accurate bending data on such small specimens would also be difficult, and while potentially useful for local bending moment-curvature behavior, the true stress–strain behavior could still only be inferred indirectly. Furthermore, the specimen in the experiment exhibited noticeable shakedown behavior (as is commonly seen in uniaxial experiments of Nitinol, at least for initial loading cycles), and some permanent strain existed as the strain increments were increased. Nevertheless, experimental work to independently obtain meaningful material property data on individual ligaments will be pursued in the future.

Consequently, we chose cycle 6 of Fig. 19(b), taken to 30% strain, to simulate and performed several trial simulations with different material laws to calibrate Model 3. We recognize that our uniaxial constitutive model contains a large number of parameters that can be used to fit the specimen's response, so no claim is made currently that Model 3 is necessarily the optimal one. Considering the reasonable agreement with both the mechanical response and the deformation pattern observed in Fig. 20, however, indicates that it is a credible one. Furthermore, Model 3 has certain expected features of NiTi behavior, namely asymmetric tension–compression behavior with lower transformation stresses and larger transformation strains in tension vs. compression, yet both having positive tangent moduli consistent with material that has experienced some shakedown cycling. Overall, we believe we can proceed with some confidence to investigate the effects of boundary conditions and geometric imperfections.

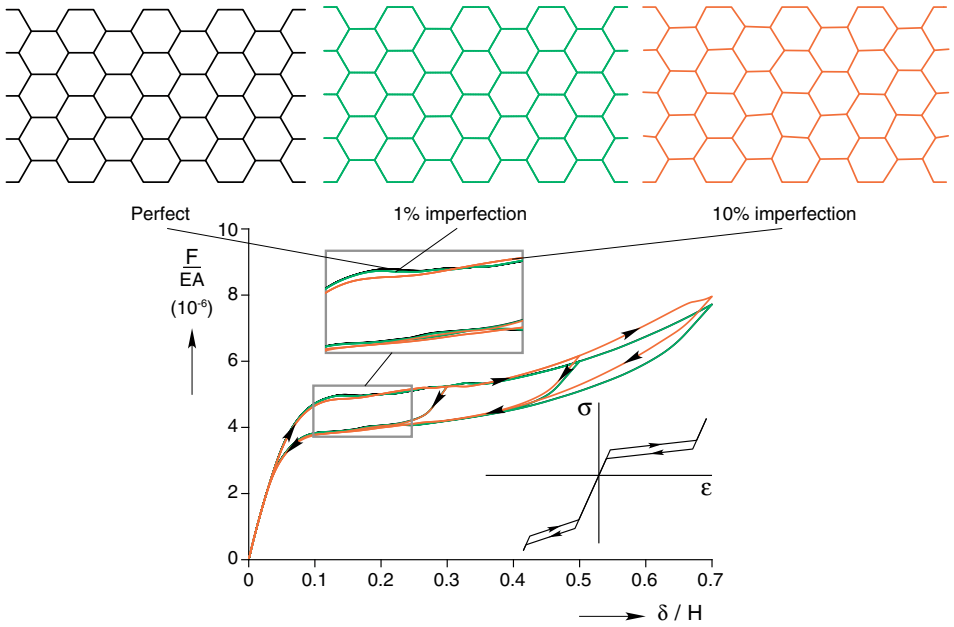

Fig. 18. Comparison of compressive loading–unloading responses for finite perfect and imperfect honeycombs ($\zeta = 0, 0.01, 0.1$) with an asymmetric, hysteretic constitutive response (Model 2).

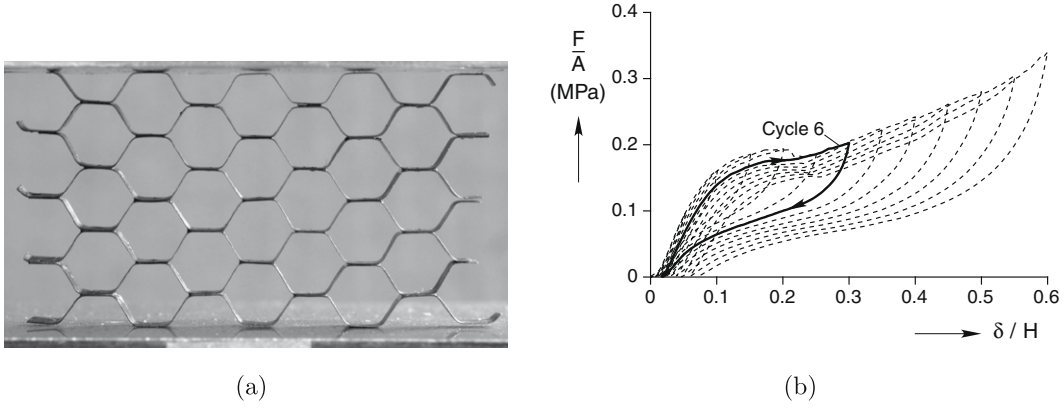

Fig. 19. (a) Photograph of Nitinol honeycomb specimen. (b) Experimental isothermal compressive, displacement-controlled response subjected to load–unload cycles in progressively larger 5% strain increments (data taken from Fig. 5 of Shaw et al. (2007b).)

Another "sticky" issue is the potential effects of platen-honeycomb friction at the top and bottom of the specimen, so friction was included in the simulations. A friction coefficient of $\mu = 0.3$ was chosen such that the response of the finite, imperfect honeycomb reasonably matched the experimental results. This value is considered realistic for the dry, steel platens used. The same model was simulated frictionless, in order to quantify the effect of friction as well as to be comparable to the finite sample results presented earlier. A frictional or standard contact algorithm was used for the two cases, respectively, since the actual honeycomb top and bottom surfaces were not precisely planar, causing some cells to contact the platens before others at the initiation of loading. This was the cause of the concave curvature and delayed upturn in the experimental response near $\delta/H = 0.01$, as settling occurs between the honeycomb top/bottom ends and the platens. After this "slack" was exhausted the structure stiffened to a roughly linear response up to about $\delta/H = 0.05$.

The case of $\mu = 0.3$ results in quite satisfactory agreement with the experimental response as seen in Fig. 20(a). Not surprisingly, the presence of friction acts to stiffen the overall response as shown in the three responses of finite, imperfect honeycombs. The response of the infinite-perfect honeycomb is also shown for comparison, being the stiffest of the structures considered. Obviously, the presence of imperfections is a strong effect, softening the response considerably compared to the perfect case. All cases were stable for their entire paths for this choice of constitutive law (Model 3). The case of $\mu = 0.3$ for the finite, imperfect honeycomb fits the experimental results very well, except for a minor deviation near $\delta/H = 0.2$ during loading. Similarities are also apparent in Fig. 20(b) between the simulated ($\mu = 0.3$) and experimental configurations near the maximum strain, $\delta/H = 0.3$. The overall shapes are roughly trapezoidal with cells flattened at the top, although the distortion is somewhat more severe in the experiment. Notice that the center cell in the bottom row is relatively undeformed in both cases. Overall, we consider the agreement between the simulation and experimental results to be quite satisfactory.

5. Summary and conclusions

The recently discovered method for bonding NiTi strips has enabled the fabrication of thin-walled SMA honeycomb, preserving the shape memory and superelastic properties of the material.

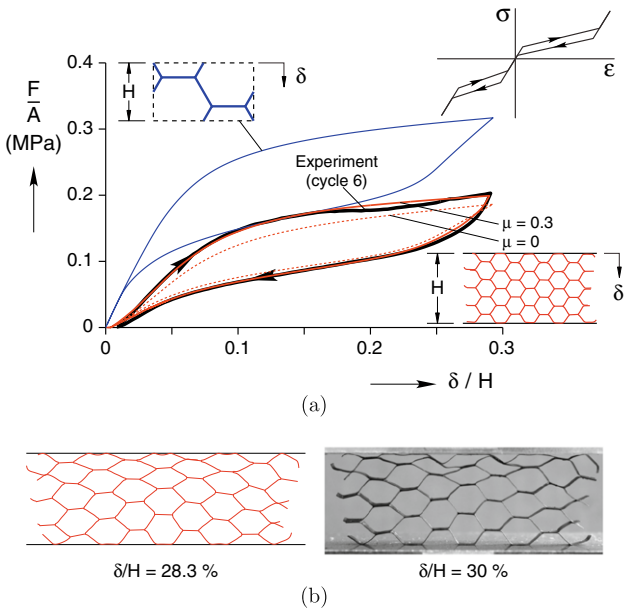

Fig. 20. (a) Macroscopic load–unload stress–strain responses: experimental measurement from cycle 6 of Fig. 19(b) (bold line) and FEM simulations (actual geometry using Model 3) with two values of friction coefficient, $\mu = 0$ (dotted line), $\mu = 0.3$ (thin solid line). The infinite-perfect honeycomb (upper left inset) principal path (thin line) is also shown for comparison. (b) Simulated configuration ($\mu = 0.3$) and experimental image near 30% strain.

The high surface area per mass cellular architecture results in remarkable enhancement (over the monolithic case) of the macroscopic superelastic and shape memory effect, as recent experiments on SMA honeycomb specimens have shown.

In this paper we presented an in-depth numerical study of the response of hexagonal SMA honeycombs subjected to large macroscopic strain, isothermal compression of varying amplitudes. Simulation and stability analyses were performed using a standard incremental algorithm in a finite element-based simulation tool with large displacement, small strain (nonlinear) kinematics, and an isothermal superelastic SMA material model. The study showed how key parameters of the local uniaxial constitutive law, such as nucleation strain, phase transformation tangent modulus, and hysteresis amplitude, influence principal responses of the bulk honeycomb (of infinite extent) and finite honeycombs with initially perfect and imperfect geometries. An investigation of the stability of the periodic unit-cell solution for the infinite structure using Bloch waves provided a key to understanding the response of finite size specimens, which showed interesting transitions from regular (almost periodic) deformations to localized cell deformations and then back to regular patterns upon continuous loading (or unloading) paths. We found that bifurcation points at the onset λ_c and termination λ_C of instability, i.e., the critical points of an unstable region in the primary path of the cell-periodic solutions, were associated with long wavelength modes for all cases considered, while intermediate unstable equilibrium points were associated with an array of finite wavelength modes. These rather remarkable potential changes of stability of the macroscopic response – due to the SMA's inherent softening during stress-induced phase transformation and then stiffening upon phase saturation – has important implications, since they can cause equilibrium solutions to deviate from the periodic, or nearly periodic, configurations for significant portions of their loading path.

Finally, we demonstrated that our simulation tool can be well calibrated to experimental results, using a material model that captures the uniaxial tension–compression asymmetry (necessary to properly capture the dominate bending effects of cell walls) and modeling some frictional effects at the loading platens. Beside capturing the overall mechanical response, the simulation tool presented has obvious utility to capture deformed configurations to identify worst case stresses/strains. This helps to quantify the local-to-global strain amplification (structural performance) and determine potential failure locations (structural reliability). Although the present investigation pertains to specific cell geometry and load direction, the rich behavior demonstrated can be potentially altered by changing the load orientation and cell geometry, thus opening new avenues for interesting design problems and novel applications of such light-weight, cellular, adaptive structures. We look forward to using the simulation tool in design optimization and performance predictions of other honeycomb cell geometries and loading directions in the future, as well as generalizing the material model to include thermo-mechanical coupling to capture loading rate effects and the shape memory effect.

Acknowledgements

The authors gratefully acknowledge the financial support from the National Science Foundation, Award CMS0409084 (program manager Dr. Ken Chong), and the U.S. Air Force Office of Scientific Research, Award FA9550-08-1-0313 (program manager Dr. Les Lee).

References

Ashby, M., Evans, A., Fleck, N., Gibson, L., Hutchinson, J., Wadley, H., 2000. Metals Foams: A Design Guide, first ed. Butterworth–Heinemann, Boston, MA.

FEAP, 2005. User Manual, seventh ed. University of California at Berkeley (Civil and Environmental Engineering) and the University of Michigan (Aerospace Engineering).

Freed, Y., Aboudi, J., Gilat, R., 2008. Investigation of shape memory alloy honeycombs by means of a micromechanical analysis. Modelling and Simulation in Materials Science and Engineering 16 (5), 055002 (22pp). http://stacks.iop.org/0965-0393/16/055002.

Gall, K., Sehitoglu, H., Chumlyakov, Y., Kireeva, I., 1999. Tension–compression asymmetry of the stress–strain response in aged single crystal and polycrystalline NiTi. Acta Materialia 47 (4), 1203–1217.

Geymonat, G., Mueller, S., Triantafyllidis, N., 1993. Homogenization of nonlinearly elastic materials, microscopic bifurcation and macroscopic loss of rank-one convexity. Archive of Rational Mechanics and Analysis 122, 231–290.

Gibson, L.J., Ashby, M.F., 1997. Cellular Solids: Structure and Properties, 2nd ed.. Cambridge Solid State Series Cambridge University Press, Cambridge, UK.

Grummon, D., Shaw, J., Foltz, J., 2006. Fabrication of cellular shape memory alloy materials by reactive eutectic brazing using niobium. Materials Science and Engineering A, 1113–1118.

Grummon, D.S., Shaw, J.A., Gremillet, A., 2002. Low-density open-cell foams in the NiTi system. Applied Physics Letters 82 (16), 2727–2729.

Hassan, M.R., Scarpa, F.L., Mohamed, N.A., 2004. Shape memory alloys honeycomb: design and properties. In: Lagoudas, D.C. (Ed.), Proceedings of SPIE: Smart Structures and Materials 2004: Active Materials: Behavior and Mechanics. Vol. 5387. SPIE, pp. 557–564. http://link.aip.org/link/?PSI/5387/557/1.

Hill, R., 1958. A general theory of uniqueness and stability in elastic–plastic solids. Journal of the Mechanics and Physics of Solids 6, 236–249.

Iadicola, M.A., Shaw, J.A., 2004. Rate and thermal sensitivities of unstable transformation behavior in a shape memory alloy. International Journal of Plasticity 20, 577–605.

Lagoudas, D.C., Vandygriff, E.L., 2002. Processing and characterization of NiTi porous sma by elevated pressure sintering. Journal of Intelligent Material Systems and Structures 13, 837–850.

Li, B.-Y., Rong, L.-J., Luo, X.-H.Y.-Y.L., 1999. Transformation behavior of sintered porous NiTi alloys. Metallurgical and Materials Transactions 30A, 2753–2756.

Okabe, Y., Minakuchi, S., Shiraishi, N., Murakami, K., Takeda, N., March 2008. Smart honeycomb sandwich panels with damage detection and shape recovery functions. Advanced Composite Materials 17, 41–56. http://dx.doi.org/10.1163/156855108X295645.

Papka, S., Kyriakides, S., 1994. In-plane compressive response of crushing of honeycomb. Journal of the Mechanics and Physics of Solids 42, 1499–1532.

Shaw, J.A., Churchill, C., Triantafyllidis, N., Michailidis, P., Grummon, D., Foltz, J., 2007a. Shape memory alloy honeycombs: Experiments and simulation. In: Proceedings of the AIAA/ASME/ASCE/AHS/ASC Structures, Structural Dynamics and Materials Conference. Vol. 1. Waikiki, HI, United States, pp. 428–436.

Shaw, J.A., Grummon, D.S., Foltz, J., 2007b. Superelastic NiTi honeycombs: Fabrication and experiments. Smart Materials and Structures 16, S170–S178.
Shaw, J.A., Kyriakides, S., 1995. Thermomechanical aspects of NiTi. Journal of the Mechanics and Physics of Solids 43 (8), 1243–1281.
Shaw, J.A., Kyriakides, S., 1997. On the nucleation and propagation of phase transformation fronts in a NiTi alloy. Acta Materialia 45 (2), 683–700.
Triantafyllidis, N., Nestorović, M.D., Schraad, M.W., 2006. Failure surfaces for finitely strained two-phase periodic solids under arbitrary plane strains. Journal of Applied Mechanics 73, 505–515.
Triantafyllidis, N., Samanta, S.K., 1986. Bending effects on flow localization in metallic sheets. Proceedings of the Royal Society of London A406, 205–226.
Triantafyllidis, N., Schnaidt, W.C., 1993. Comparison of microscopic and macroscopic instabilities in a class of two-dimensional periodic composites. Journal of the Mechanics and Physics of Solids 41, 1533–1565.
Triantafyllidis, N., Schraad, M.W., 1998. Onset of failure in aluminum honeycombs under general in-plane loading. Journal of the Mechanics and Physics of Solids 46, 1089–1124.